

2020

## Significance of Gravitational Nonlinearities on the Dynamics of Disk Galaxies

Alexandre Deur

Corey Sargent  
*Old Dominion University, cjsargen@odu.edu*

Balša Terzić  
*Old Dominion University, bterzic@odu.edu*

Follow this and additional works at: [https://digitalcommons.odu.edu/physics\\_fac\\_pubs](https://digitalcommons.odu.edu/physics_fac_pubs)



Part of the [External Galaxies Commons](#)

---

### Original Publication Citation

Deur, A., Sargent, C., & Terzić, B. (2020, Jun). Significance of gravitational nonlinearities on the dynamics of disk galaxies. *Astrophysical Journal*, 896(2), 11, Article 94. <https://doi.org/10.3847/1538-4357/ab94b6>

This Article is brought to you for free and open access by the Physics at ODU Digital Commons. It has been accepted for inclusion in Physics Faculty Publications by an authorized administrator of ODU Digital Commons. For more information, please contact [digitalcommons@odu.edu](mailto:digitalcommons@odu.edu).



# Significance of Gravitational Nonlinearities on the Dynamics of Disk Galaxies

Alexandre Deur<sup>1</sup> , Corey Sargent<sup>2</sup> , and Balša Terzić<sup>2</sup> <sup>1</sup> Department of Physics, University of Virginia, Charlottesville, VA 22901, USA<sup>2</sup> Department of Physics, Old Dominion University, Norfolk, VA 23529, USA; [bterzic@odu.edu](mailto:bterzic@odu.edu)

Received 2020 January 10; revised 2020 May 17; accepted 2020 May 18; published 2020 June 17

## Abstract

The discrepancy between the visible mass in galaxies or galaxy clusters and that inferred from their dynamics is well known. The prevailing solution to this problem is dark matter. Here we show that a different approach, one that conforms to both the current standard model of particle physics and general relativity (GR), explains the recently observed tight correlation between the galactic baryonic mass and the measured accelerations in the galaxy. Using direct calculations based on GR's Lagrangian and parameter-free galactic models, we show that the nonlinear effects of GR make baryonic matter alone sufficient to explain this observation. Our approach also shows that a specific acceleration scale dynamically emerges. It agrees well with the value of the MOND acceleration scale.

*Unified Astronomy Thesaurus concepts:* [Dark matter \(353\)](#); [General relativity \(641\)](#); [Spiral galaxies \(1560\)](#)

## 1. Introduction

An empirical tight relation between accelerations calculated from the galactic baryonic content and the observed accelerations in galaxies has been reported by McGaugh et al. (2016, hereafter [MLS2016](#)); larger accelerations are accounted for by the baryonic matter, i.e., there is no missing mass problem, while in lower-acceleration regions, dark matter or gravitational/dynamical laws beyond Newton's are necessary. This correlation is surprising because galactic dynamics should be dictated by the total mass (believed to be predominantly dark), but instead, the baryonic mass information alone is sufficient to get the observed acceleration. A tight connection between dark and baryonic matter distributions would explain the observation, but such a connection has not been expected. While the relation from [MLS2016](#)—including its small scatter—can be reproduced with dark matter models (Ludlow et al. 2017), the consistency of the measured correlation width with the observational uncertainties suggests a dynamical origin rather than an outcome of galaxy formation, since this would add an extra component to the width.

Dynamical studies of galaxies typically use Newton's gravity. However, it has been argued that once galactic masses are considered, relativistic effects arising from large masses (rather than large velocities) may become important (Deur 2009, 2017, 2019). Their physical origin is that in general relativity (GR), gravity fields self-interact. In this article, we explore whether these effects can explain the relation in [MLS2016](#) without requiring dark matter or modifying gravitation as we currently know it.

The article is organized as follows. We first outline the self-interaction effects in GR, then discuss in Section 3 the empirical tight dependence of observed acceleration on baryonic mass in disk (i.e., lenticular and spiral) galaxies. In Section 4, we use GR's equations to compute the correlation. These CPU-intensive calculations allow us to study only a few galaxies, modeled as bulgeless disks. To cover the full range of disk galaxy morphologies, including those with a significant

bulge, in Section 5 we develop two dynamical models of disk galaxies in different but complementary ways: uniform sampling (Section 5.1) and random sampling (Section 5.2) of the galactic parameter space. In Section 6 we show the results from these models and compare them to observations. Finally, in Section 7, we summarize our findings and their importance.

## 2. Self-interaction Effects in GR

Field self-interaction makes GR nonlinear. The phenomenon is neglected when Newton's law of gravity is used, as is typically done in dynamical studies of galaxies or galaxy clusters. However, such a phenomenon becomes significant once the masses involved are large enough. Furthermore, it is not suppressed by low velocity—unlike some of the more familiar relativistic effects—as revealed by, e.g., the inspection of the post-Newtonian equations (Einstein et al. 1938). In fact, the same phenomenon exists for the strong nuclear interaction and is especially prominent for slow-moving quark systems (heavy hadrons), in which case, it produces the well-known quark confining linear potential.

The connection between self-interaction and nonlinearities is seen, e.g., by using the polynomial form of the Einstein–Hilbert Lagrangian (see, e.g., Salam 1974; Zee 2013),

$$\mathcal{L} = \frac{\sqrt{\det(g_{\mu\nu})} g_{\mu\nu} R^{\mu\nu}}{16\pi G} = \sum_{n=0}^{\infty} (16\pi GM)^{n/2} [\varphi^n (\partial\varphi\partial\varphi - (16\pi GM)^{1/2} \varphi T)], \quad (1)$$

where  $g_{\mu\nu}$  is the metric,  $R_{\mu\nu}$  is the Ricci tensor,  $T_{\mu\nu}$  is the energy-momentum tensor,  $M$  is the system mass, and  $G$  is the gravitational constant. In the natural units ( $\hbar = c = 1$ ) used throughout this article,  $[G] = \text{energy}^{-2}$ . The polynomial is obtained by expanding  $g_{\mu\nu}$  around a constant metric  $\eta_{\mu\nu}$  of choice, with  $\varphi_{\mu\nu} \equiv g_{\mu\nu} - \eta_{\mu\nu}$  the gravitational field. The brackets are shorthand for sums over Lorentz-invariant terms (Deur 2017). For example, the  $n = 0$  term is explicitly given

by the Fierz–Pauli Lagrangian (Fierz & Pauli 1939):

$$[\partial\varphi\partial\varphi - \sqrt{16\pi GM}\varphi T] = \frac{1}{2}\partial^\lambda\varphi_{\mu\nu}\partial_\lambda\varphi^{\mu\nu} - \frac{1}{2}\partial^\lambda\varphi_\mu^\mu\partial_\lambda\varphi_\nu^\nu - \partial^\lambda\varphi_{\lambda\nu}\partial_\mu\varphi^{\mu\nu} + \partial^\nu\varphi_\lambda^\lambda\partial^\mu\varphi_{\mu\nu} - \sqrt{(16\pi GM)}\varphi^{\mu\nu}T_{\mu\nu}.$$

While Equation (1) is often used to study quantum gravity—with questions raised regarding its applicability in that context, see, e.g., Padmanabhan (2008)—we stress that the calculations and results presented here are classical and thus not subject to the difficulties arising from quantum gravity or the issues raised in Padmanabhan (2008). Field self-interaction originates from the  $n > 0$  terms in Equation (1), distinguishing GR from Newton’s theory, for which the Lagrangian is given by the  $n = 0$  term. One consequence of the  $n > 0$  terms is that they effectively increase gravity’s strength. It is thus reasonable to investigate whether they may help to solve the missing mass problem. In fact, it was shown that they allow us to quantitatively reproduce the rotation curves of galaxies without need for dark matter, also providing a natural explanation for the flatness of the rotation curves (Deur 2009).

The phenomenon underlying these studies is ubiquitous in quantum chromodynamics (QCD; the gauge theory of the strong interaction). The GR and QCD Lagrangians are similar in that they both contain field self-interaction terms. In fact, they are topologically identical (see Appendix A where the similarities and differences between GR and QCD are discussed). In QCD, the effects of field self-interaction are well known, as they are magnified by the large QCD coupling, typically  $\alpha_s \simeq 0.1$  at the transition between perturbative and strong regimes (Deur et al. 2016).

In GR, self-interaction effects become important when  $GM$ —which, in the natural unit used in this manuscript, has a length dimension—reaches a fraction of the characteristic length  $L$  of the system. Numerical lattice calculations show that  $GM \approx 10^{-3}L$  characterizes systems where self-interaction cannot be neglected (Deur 2017). At the particle level, gravity and, a fortiori, its nonlinearities are automatically ignored, since  $GM_p \approx 10^{-39}r_p$  ( $M_p$  and  $r_p$  are the proton mass and radius, respectively), and hence  $GM_p/r_p/\alpha_s \approx 10^{-40}$ . However, the ratio becomes  $10^{-2}$  for galactic systems, making it reasonable to ask whether QCD-like GR’s self-interaction effects should be considered. That value characterizes, e.g., typical disk galaxies, galaxies interacting in a cluster, and the Hulse–Taylor binary. A large mass discrepancy is apparent when the dynamics of galaxies and galaxy clusters are analyzed, while the Hulse–Taylor binary is already known to be governed by strong gravity.

In QCD, a critical effect of self-interaction is a stronger binding of quarks, resulting in their confinement. In GR, self-interaction likewise increases gravity’s binding, which can provide an origin for the missing mass problem. However, one may question the relevance of field self-interaction at large galactic radii  $r$ . At these distances, the missing mass problem is substantial, while the small matter density should make the self-interaction effects negligible. The answer is in the behavior of the gravitational field lines; once they are distorted at small  $r$  due to the larger matter density, they evidently remain so even if the matter density becomes negligible (no more field self-interaction, i.e., no further distortion of the field lines), preserving a form of potential different from that of Newton.

Thus, even if the gravity field becomes weak, the deviation from Newton’s gravity remains.<sup>3</sup>

A key feature for this article is the suppression of self-interaction effects in isotropic and homogeneous systems (Deur 2009):

1. In a two-point system, large  $\sqrt{GM}$  or  $\alpha_s$  values lead to a constant force between the two points (and a vanishing force elsewhere), i.e., the stringlike flux tube that is well known in QCD.
2. Due to the symmetry of a homogeneous disk, the flux collapses only outside of the disk plane, thereby confining the force to two dimensions. Consequently, the force between the disk center and a point in the disk at a distance  $r$  decreases as  $1/r$ .
3. For a homogeneous sphere, the force recovers its usual  $1/r^2$  behavior, since the flux has no particular direction or plane of collapse.

This symmetry dependence has led to the discovery of a correlation between the missing mass of elliptical galaxies and their ellipticity (Deur 2014). This also illustrates the point of the previous paragraph: even if the matter density in the disk decreases quickly with  $r$ , the missing mass problem—which, in our approach, comes from the difference between the GR and Newtonian treatments—grows worse, since the difference between the  $1/r$  GR force in the 2D disk and the  $1/r^2$  Newtonian force grows with  $r$ . This offers a simple explanation for the relation reported in MLS2016: although densities, and thus accelerations, are largest at small  $r$ , the  $1/r - 1/r^2$  difference between the GR and Newtonian treatments remains moderate. However, the difference becomes important at large  $r$ , where accelerations are small. Furthermore, at small  $r$ , the  $1/r^2$  force is recovered for GR due to finite disk thickness  $h_z$ , since isotropy is restored for  $r \lesssim h_z$ . This recovery is amplified, since disk galaxies often contain a central high-density bulge that is usually nearly spherical (Méndez-Abreu et al. 2008). The departure from the  $1/r^2$  behavior then occurs after the bulge–disk transition.

### 3. Baryonic Mass–Acceleration Dependence

The correlation between the radial acceleration traced by rotation curves ( $g_{\text{obs}}$ ) and that predicted by the known distribution of baryons ( $g_{\text{bar}}$ ) reported in MLS2016 was established after analyzing 2693 points in 153 disk galaxies with varying morphologies, masses, sizes, and gas fractions. The MLS2016 authors found a good functional form fitting the correlation:

$$g_{\text{obs}} = \frac{g_{\text{bar}}}{1 - e^{-\sqrt{g_{\text{bar}}/g_{\ddagger}}}}, \quad (2)$$

where  $g_{\ddagger}$  is an acceleration scale, the only free parameter of the fit. In the remainder of this paper, we show that the observed correlation may be entirely due to the nonlinear GR effects that are neglected in the traditional Newtonian analysis. In the next section, we use a direct GR calculation of rotation curves for actual galaxies modeled as bulgeless disks (Deur 2009). We

<sup>3</sup> An analogous phenomenon exists for QCD: the parton distribution functions (PDFs) that characterize the structure of the proton are nonperturbative objects even if they are defined and measured in the limit of the asymptotic freedom of quarks where  $\alpha_s$  tends to zero. Thus, PDFs are entirely determined by the self-interaction/nonlinearities of QCD, although those are negligible at the large energy-momentum scale where PDFs are relevant.

show that when the galactic bulge of the actual galaxy is negligible, the calculation yields a relation that agrees with the empirical correlation from [MLS2016](#). In the two subsequent sections, we develop models to include the effect of bulges and account for the variation of the morphology of disk galaxies.

#### 4. Direct Calculations

The rotation curves of several disk galaxies were computed in [Deur \(2009\)](#) based on Equation (1) and using numerical lattice calculations in the static limit ([Deur 2017](#)). The method is summarized in Appendix B. The two-body lattice calculations described there show that given the magnitude of galactic masses, the self-interaction traps the field. For a two-body system, i.e., a system characterized by one dominant dimension, field trapping results in a constant force, since a force magnitude at a given distance  $r$  is proportional to the field line density crossing an elementary surface. Thus, for 1D systems, the force is constant and the potential grows linearly with the distance  $r$ , as obtained in the numerical lattice calculations ([Deur 2009, 2017](#)). We can extend this result to a 2D system such as a disk. For a field restricted to two dimensions, the flux disperses over an angle rather than a solid angle, which yields a force that varies as  $1/r$ , i.e., obeys a logarithmic potential. Extending the 1D result to the 2D disk case of galaxies assumes that the spread of the mass within the disk area does not compromise the trapping of the field in two dimensions. This is reasonable, since most galactic baryonic mass is concentrated near its center. This reasoning and the hypothesis that the field remains trapped for a disk are supported by a different approach that uses a mean-field method applied to a thin disk distribution ([Deur 2020](#)). The mean-field calculation yields a large-distance logarithmic potential when the mass of the disk is sufficient (see Figure B2 in Appendix B).

The calculations of [Deur \(2009\)](#) neglect the galactic bulge and approximate a spiral galaxy with a disk featuring an exponentially falling density profile. They were carried out for nearly bulgeless Hubble type 5 and 6 galaxies (NGC 2403, 3198, and 6503), and for Hubble type 3 and 4 galaxies (NGC 2841, 2903, and 7331), which have moderate bulges. Using these results, we can compute the total acceleration  $g_{SI}$  stemming from baryonic matter and including GR's field self-interaction analog of  $g_{obs}$  from [MLS2016](#). Plotting it versus the Newtonian acceleration  $g_N$  obtained from the same distribution of baryonic matter but ignoring GR's self-interaction analog of  $g_{bar}$  from [MLS2016](#), one obtains the results shown in the top panel of Figure 1. The curves for type 5 and 6 galaxies agree well with the observed correlation, thereby providing an explanation for it in bulgeless galaxies. However, the curves for type 3 and 4 galaxies, while qualitatively following the correlation, overestimate  $g_{SI}$  and lie on the edge of the observed distribution. That the empirical correlation is reproduced only for bulgeless galaxies supports that (1) the correlation from [MLS2016](#) is explainable by GR's self-interaction without requiring dark matter or modification of the known laws of nature, and (2) at large acceleration, i.e., typically for small galactic radii, the bulge reduces the value of  $g_{SI}$ , since self-interaction effects cancel for isotropically distributed matter.

Although based directly on the GR's Lagrangian, the lattice approach is limited, since it is computationally costly and applies only to simple geometry, limiting the study to only a few late Hubble type galaxies at one time. To study the correlation from [MLS2016](#) over the wide range of disk galaxy morphologies, we developed two models based on (1) the  $1/r$  gravitational force

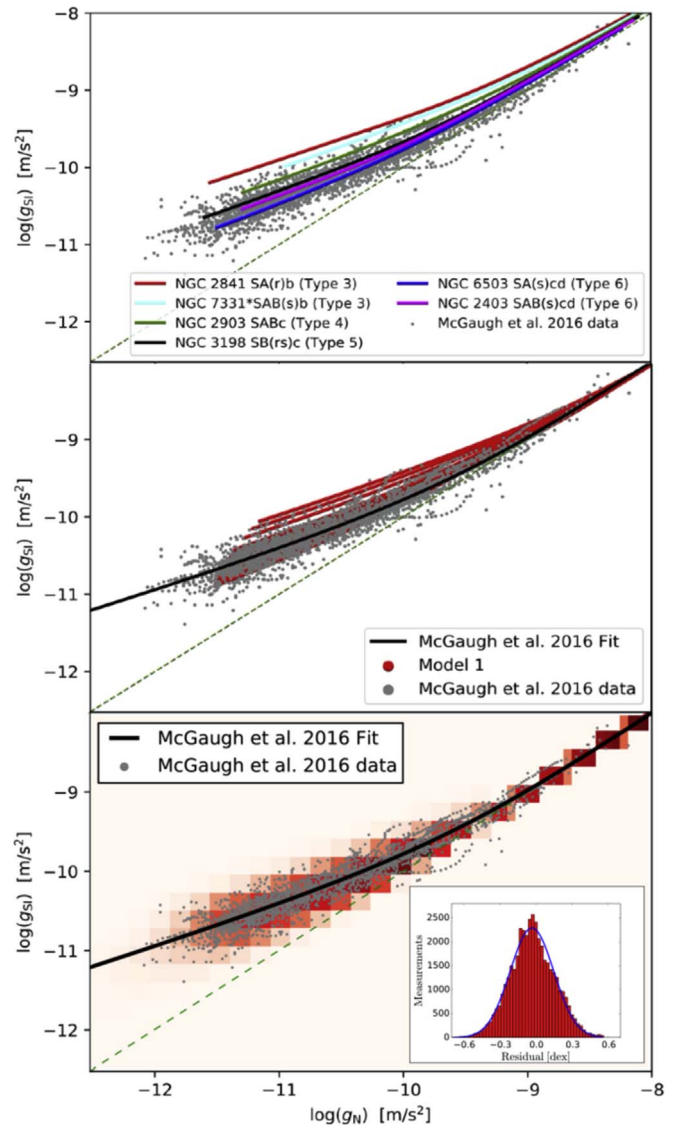


**Figure 1.** Correlation between the acceleration accounting for GR's self-interaction,  $g_{SI}$ , and the acceleration computed with Newtonian gravity,  $g_N$ , plotted along with the correlation observed in [MLS2016](#) (gray circles). Top: Lagrangian-based calculations for various Hubble type galaxies. The galaxies are approximated as pure (bulgeless) disks. The calculations agree well with the observation when this approximation is justified (type 5 and 6 galaxies) but depart gradually from the observation as the bulge becomes more important. Middle: model 1 with uniform sampling of the galactic parameter phase space. Bottom: model 2 with galactic parameter phase space sampled following observed distributions (1146 galaxies sampled at 100 radial values are shown). The density of the data points obtained with model 2 is encoded by the color scale. The dashed line indicates  $g_{SI} = g_N$ . Embedded in the bottom panel is the residual distribution between the result of model 2 and the best fit to the observational data (black line) beyond the transition radius,  $r > r_t$  (for points within the transition radius,  $r \leq r_t$ , the deviation from the [MLS2016](#) fit is, by construction, small but systematic; hence, the residual has no statistical meaning in that region).

resulting from solving Equation (1) for a disk of axisymmetrically distributed matter and (2) the expectation that GR field self-interaction effects cancel for spherically symmetric distributions, such as that of a bulge, restoring the familiar  $1/r^2$  force.

#### 5. Dynamical Models

To circumvent the limitations of the direct lattice calculation, we constructed two elementary models for disk galaxies. They both compute the acceleration including GR's self-interaction,

$g_{\text{SI}}$ , and the Newtonian acceleration due to the baryonic matter,  $g_{\text{N}}$ . Both  $g_{\text{SI}}$  and  $g_{\text{N}}$  are computed at a set of radii  $r$  from the galactic center to its outermost parts. This is carried out for galaxies with characteristics that sample the observed correlations reported in the literature.

The modeled galaxies have two components: a spherical bulge and a larger disk. Both contain only baryonic matter following the light distribution; i.e., there is no dark matter, and gas is either neglected or follows the stellar distribution.

The bulge is modeled with the projected surface brightness Sérsic profile (Sérsic 1963) used in Méndez-Abreu et al. (2008),  $I_b(R) = I_e 10^{-b_n [(R/R_e)^{1/n} - 1]}$ , where  $R$  is the projected radius,  $I_e$  is the surface brightness at the half-light radius  $R_e$ ,  $n$  is the Sérsic parameter, and  $b_n \approx 0.868n - 0.142$  (Caon et al. 1993). The internal mass density  $\rho_b(r)$ , where  $r$  is the deprojected radius, is computed from the surface brightness by numerically solving the Abel integral. Since GR's self-interaction effects cancel for isotropic homogeneous distributions, the potential in the bulge has the usual Newtonian form,  $\Phi_b(r) = GM_b^{\text{enc}}(r)/r$ , where  $M_b^{\text{enc}}(r)$  is the bulge mass enclosed within a sphere of radius  $r$ .

The disk is modeled with the usual surface brightness radial profile  $I_d(R) = I_0 e^{-R/h}$ , where  $I_0$  is the central surface brightness,  $h$  is the disk scale length, and possible effects from the disk thickness are neglected. Again, the corresponding mass density  $\rho_d(r)$  is computed from the Abel integral. Self-interaction in a homogeneous disk leads to a potential  $\Phi_d(r) = G'M_d^{\text{enc}}(r)\ln(r)$ , with  $M_d^{\text{enc}}(r)$  the disk mass enclosed within a radius  $r$  and  $G'$  the effective coupling of gravity in two dimensions, which depends on the physical characteristics of the disk (Deur 2017); see detailed discussion in Appendix C.

The quantities characterizing a galaxy—the bulge and disk masses,  $M_b$ ,  $M_d$  (from which  $\rho_{b,0}$  and  $\rho_{d,0}$  are obtained, respectively),  $R_e$ ,  $n$ , and  $h$ —span their observed ranges for S0 to Sd galaxies (Graham & Worley 2008; Méndez-Abreu et al. 2008; Sofue 2015). There are known relations between these quantities (Méndez-Abreu et al. 2008; Sofue 2015):

$$\log(R_e) = 0.91(7)\log(h) - 0.40(3), \quad (3)$$

$$\log(n) = 0.18(5)R_e + 0.38(2), \quad (4)$$

$$\log(M_d) = 0.58(32)\log(M_b) + 0.002(79). \quad (5)$$

We use values of  $R_e$  and  $M_b$  from the ranges of observed values to obtain the remaining galactic characteristics— $h$ ,  $n$ , and  $M_d$ —through Equations (3)–(5). Thus, there are no adjustable parameters in our models.

We stress that the accuracy of the empirical relations (Equations (3)–(5)) is not critical to this work, their purpose being only to provide reasonable values of the galactic parameter space we select. While the simplicity of our models would make it of limited interest for investigating the intricate peculiarities of galaxies, such simplicity is beneficial for the present study: no numerous parameters or phenomena (e.g., baryonic feedback) are needed for adjustment to reproduce the correlation from MLS2016. That the correlation emerges directly from basic models underlines the fundamental nature of the correlation.

The two dynamical models introduced in the remainder of this section share the above description. From here, they differ in two aspects. The first is in how the observed correlations in Equations (3)–(5) are implemented: model 1 enforces the correlations strictly, while model 2 allows for the parameter space to be randomly sampled. The second difference is in

representing the transition radius,  $r_t$ , between the bulge-dominated regime near the center and the disk-dominated regime: model 1 explicitly sets the transition at twice the typical bulge scale,  $r_t = 2R_e$ , while model 2 defines  $r_t$  as the radius at which the forces due to the two components—the bulge and the disk—are equal.

### 5.1. Model 1: Uniform Sampling of the Galactic Parameter Space

This model generates a galaxy set representative of disk galaxy morphologies by uniformly sampling the values of the galactic characteristics discussed in the previous section. The model strictly enforces Equations (3)–(5). This offers the advantage of simplicity, e.g., clarity, speed, and robustness. Actual correlations, however, vary in their strengths. Hence, strictly implementing a correlation between quantities  $a$  and  $b$  and another between  $a$  and  $c$  would result in quantities  $b$  and  $c$  also being correlated, while if the actual correlations between  $a$  and  $b$  and  $a$  and  $c$  are both weak, then  $b$  and  $c$  may not be correlated. For example, propagating correlations among different galactic characteristics yields an inadequate relation between  $M_b$  and  $M_d$ :  $M_d \propto M_b^{-\alpha \pm \Delta}$ , with  $\Delta \gg \alpha = 31$ . To circumvent this problem, we use  $h \propto R_e^{1.0}$ ,  $M_b \propto R_e^{0.1}$ ,  $n \propto R_e^{0.1}$ , and  $M_d \propto h^{1.0}$ , in rough agreement with the correlations from Khosroshahi et al. (2000) and Méndez-Abreu et al. (2008).

The correlations are applied strictly, i.e., without accounting for the scatter seen in actual data, since systematically spanning the observed typical ranges for the quantities contributes to the width of the correlation reported in MLS2016, and accounting for such scatter would partly double-count, and thus overestimate, the width.

Inside the spherical bulge-dominated region (denoted by subscript  $r < r_t$ ), the self-interaction cancels, and the GR and Newtonian accelerations are the same:

$$g_{\text{SI}, r < r_t}(r) = g_{\text{N}, r < r_t}(r) = \frac{G}{r^2}(M_b^{\text{enc}}(r) + M_d^{\text{enc}}(r)), \quad (6)$$

where

$$M_b^{\text{enc}}(r) = 4\pi \int_0^r \tilde{r}^2 \rho_b(\tilde{r}) d\tilde{r}, \quad (7)$$

$$M_d^{\text{enc}}(r) = 2\pi \int_0^r \tilde{r} \rho_d(\tilde{r}) d\tilde{r}. \quad (8)$$

In the disk-dominated region (denoted by subscript  $r > r_t$ ), numerical lattice calculations indicate that self-interaction leads to a collapse in the gravitational field lines (Deur 2009, 2017). The bulge density there is less significant than that of the disk, but it is still present. The total acceleration is

$$g_{\text{SI}, r > r_t}(r) = \frac{G}{r^2}M_b^{\text{enc}}(r) + \frac{G'}{r}M_d^{\text{enc}}(r). \quad (9)$$

The Newtonian acceleration  $g_{\text{N}, r > r_t}$  in this region retains the form given in Equation (6).

Here  $G'$  is determined by requiring the accelerations to match at  $r_t$ :  $g_{\text{SI}, r < r_t}(r_t) = g_{\text{SI}, r > r_t}(r_t)$ . Thus,  $G' = G/r_t$ , by construction. The justification for this choice of  $G'$  is explained in detail in Appendix C.

The accelerations in the bulge and disk regions are smoothly connected using a Fermi–Dirac function centered at  $r_t = 2R_e$  and of width  $r_t/2$ :  $D(r) = 1/(1 + e^{2(r-r_t)/r_t})$ . Therefore, the

acceleration with self-interaction is

$$g_{\text{SI}}(r) = D(r)g_{\text{SI},r < r_t}(r) + (1 - D(r))g_{\text{SI},r > r_t}(r), \quad (10)$$

while the Newtonian acceleration is

$$g_{\text{N}}(r) = \frac{G}{r^2}(M_b^{\text{enc}}(r) + M_d^{\text{enc}}(r)). \quad (11)$$

The choice of width value for  $D(r)$  has little influence on the result; abruptly transitioning between bulge and disk, i.e., using a step function rather than  $D(r)$ , yields quantitatively similar results. The small dependence on the functional form for the transition is also supported by the agreement between models 1 and 2, which use different methods for the transition, as we discuss next.

### 5.2. Model 2: Random Sampling of the Galactic Parameter Space

For model 2, we randomly generate the galaxy characteristics with Gaussian distributions centered at the observed parameter values and of widths determined by the observed distributions. In order to sample a realistic galaxy parameter space, we apply two types of cuts on the generated galaxy characteristics. The first type of cut ensures that the randomly sampled galaxy characteristics simultaneously satisfy Equations (3)–(5). A candidate galaxy is generated by first randomly sampling distributions of  $R_e$  and  $M_b$  separately and then using them to randomly sample the observed correlations in Equations (3)–(5) to obtain  $h$ ,  $n$ , and  $M_d$ . These are then combined to find  $\rho_{b,0}$  and  $\rho_{d,0}$ , thereby completing the parameter set for a single candidate galaxy. This particular candidate galaxy then passes the first cut if its characteristics satisfy all of the correlations to within one standard deviation. Galaxies that pass this first cut are shown as orange and red circles in Figure 2. The second type of cut is outlined below.

The transition between the bulge-dominated and the disk-dominated regions is implemented with a step function  $H(x) = 1$  for  $x < 0$ , and zero otherwise, such that at  $r_t$ , the acceleration is kept continuous by the proper choice of  $G'$ . The transition radius  $r_t$  is defined as the radial location at which the acceleration due to the disk alone is equal to that due to the bulge alone,

$$G \frac{M_b^{\text{enc}}(r_t)}{r_t^2} = G' \frac{M_d^{\text{enc}}(r_t)}{r_t}, \quad (12)$$

with  $G' = G/r_t$  (see Appendix C). This choice of  $G'$  simplifies the condition for the transition  $r_t$  to

$$M_b^{\text{enc}}(r_t) = M_d^{\text{enc}}(r_t). \quad (13)$$

Some bulge-dominated galaxies will not have such a transition within  $r = 100$  kpc and are removed from the sample. This is the second type of cut applied on the parameter space. Galaxies that pass both the first and the second types of cuts are shown as red circles in Figure 2. Essentially, orange circles denote galaxies that are largely bulge-dominated and thus cannot qualify as disk galaxies. Red circles represent galaxies having small-to-moderate bulges that qualify them as disk galaxies.

Models 1 and 2 use different methods for the bulge–disk transition. The agreement between the two models suggests that they are indifferent to a particular method. The acceleration

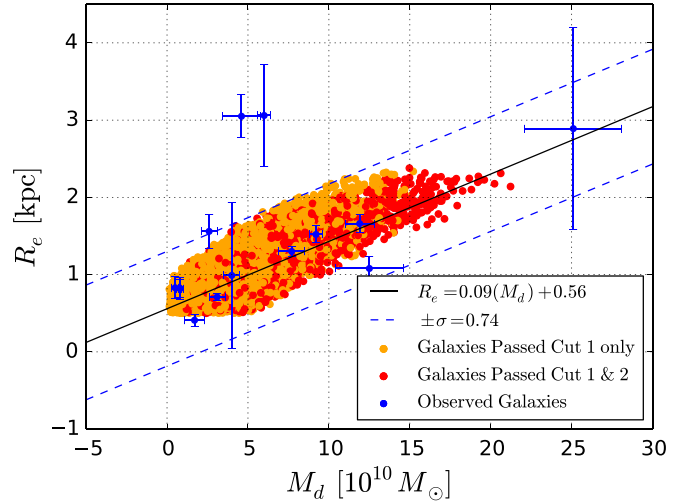


**Figure 2.** Shown is  $R_e$  vs.  $M_d$ . Observed values are shown as blue circles (Sofue 2015). The best  $\chi^2$  fit to the observed data is denoted with a solid line and 1 dex in dashed lines. Orange circles denote generated galaxies that passed the first cut only, while red circles denote those that passed both cuts. The galaxies represented by the red circles are disk galaxies, while those corresponding to the orange circles are too bulge-dominated to qualify as such.

including self-interaction is

$$g_{\text{SI}}(r) = H(r - r_t)g_{\text{SI},r < r_t}(r) + (1 - H(r - r_t))g_{\text{SI},r > r_t}(r), \quad (14)$$

where  $g_{\text{SI},r < r_t}(r)$  and  $g_{\text{SI},r > r_t}(r)$  are given in Equations (6)–(9) and  $g_{\text{N}}(r)$  in Equation (11).

In model 2, we also modeled the effect of the bulge being spheroidal rather than spherical by introducing a polar dependence,  $\rho_b(r, \phi) = \rho_b(r)(1 - \epsilon \cos^2 \phi)$ , with  $\rho_b(r)$  the spherical bulge density used in models 1 and 2. This refinement did not noticeably change the results, thereby further proving their robustness.

## 6. Results

### 6.1. Comparison with Observations

Direct lattice calculation and the two dynamical models allow us to compute the accelerations for a set of galaxies whose characteristics follow the typical observed ranges for disk galaxies. The acceleration including nonlinear self-interaction ( $g_{\text{SI}}$ ) is plotted in Figure 1 versus the acceleration computed with the same baryonic mass distribution but assuming Newtonian gravity ( $g_{\text{N}}$ ). This is compared to the observed correlation between  $g_{\text{obs}}$  and  $g_{\text{bar}}$  reported in MLS2016. The top panel shows the results for the direct calculation, the middle panel the results for model 1, and the bottom panel the results for model 2. Since model 2 samples the full parameter space selected by the cuts but with statistical weights favoring the more probable parameter space loci, the results must be plotted as data point densities, the higher densities being indicated by the darker colors. Our computed correlations agree well with the empirical observation without invoking dark matter or new laws of gravity/dynamics. To quantitatively assess this agreement, we averaged  $g_{\text{SI}}$  over all galaxies and also performed a fit of our simulated data<sup>4</sup> using

<sup>4</sup> The fit and average are performed on the data simulated with model 2 only. Since model 1 samples the galactic phase space uniformly rather than using normal distributions, a statistical analysis of it would have little meaning.

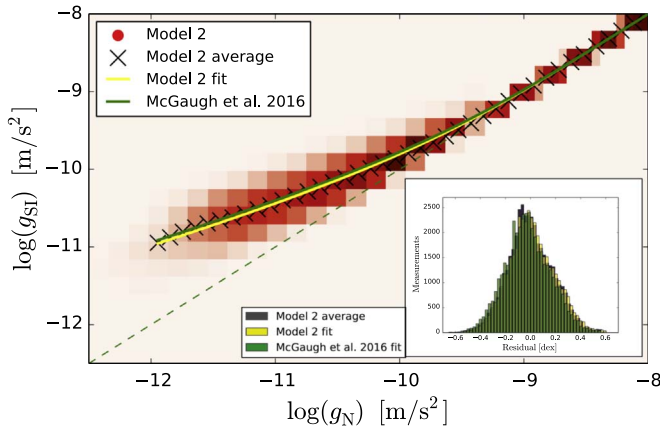


**Figure 3.** Acceleration accounting for GR’s self-interaction,  $g_{\text{SI}}$ , vs. that computed with Newtonian gravity,  $g_{\text{N}}$ . The yellow line shows the best fit to our data simulated with model 2 (red color density plot) using the form in Equation (2). The black crosses are the average  $\langle \log(g_{\text{SI}}) \rangle$ . The yellow line and crosses can be compared to the **MLS2016** fit, shown by the green line. The inset displays the residual between our simulated data and the **MLS2016** fit (green histogram, already shown in Figure 1), the one using our fit (yellow histogram), and the one using  $\langle g_{\text{SI}} \rangle$  (black histogram).

the same form used in **MLS2016**, i.e., Equation (2). The best fit and the average  $\langle \log(g_{\text{SI}}) \rangle$  versus  $\log(g_{\text{N}})$  are shown in Figure 3. Our fit parameter  $g_{\dagger}^{\text{Mod}2} = 9.71 \pm 0.27 \times 10^{-11} \text{ m s}^{-2}$  is compatible with that of **MLS2016**,  $g_{\dagger} = 1.20 \pm 0.02(\text{stat}) \pm 0.24(\text{syst}) \times 10^{-10} \text{ m s}^{-2}$ . This consistency also manifests in the nearly overlapping residuals displayed in the inset of Figure 3. This quantitatively demonstrates the agreement between our model and the data reported in **MLS2016**. We must remark that, despite this good agreement,  $g_{\dagger}^{\text{Mod}2}$  was not optimized to fit those of **MLS2016**, but it results directly from model 2 as described in Section 5.2. In fact, it cannot be adjusted, since our models have no free parameters.

### 6.2. Emerging Characteristic Acceleration Scale

The transition scale between the two regimes in model 2 is defined as the location where forces from the bulge and disk are equal; see Equation (12). The acceleration at the transition is shown in Figure 4, in which the distribution peaks at  $a(r_t) = 1.25 \pm 0.06 \times 10^{-10} \text{ m s}^{-2}$ . The sharp peaking indicates that its mode can define a characteristic transition acceleration. In our model 2, this one is consistent with the acceleration parameter  $a_0 \approx 1.2 \times 10^{-10} \text{ m s}^{-2}$  in the MOND theory (Milgrom 1983). Thus,  $a_0$  can be explained as the acceleration at the radius where the self-interaction effects become important, that is, in the context of our present model, where the disk mass overtakes the bulge mass and causes a transition from the  $1/r^2$  3D force to the  $1/r$  2D force. For bulgeless disk galaxies,  $r_t$  emerges dynamically (see discussion in Appendix C, and a direct calculation is necessary to obtain it.

### 6.3. Systematic Studies of the Residual Width

One important finding of **MLS2016** is that the width of their observed correlation is compatible with the uncertainty on the data. This poses a problem for a natural dark matter explanation, since the baryonic matter–dark matter feedback mechanisms that would be necessary to correlate baryonic and dark matter distributions would partly depend on the history of the galaxy formation, as shown in **MLS2016**. In the present

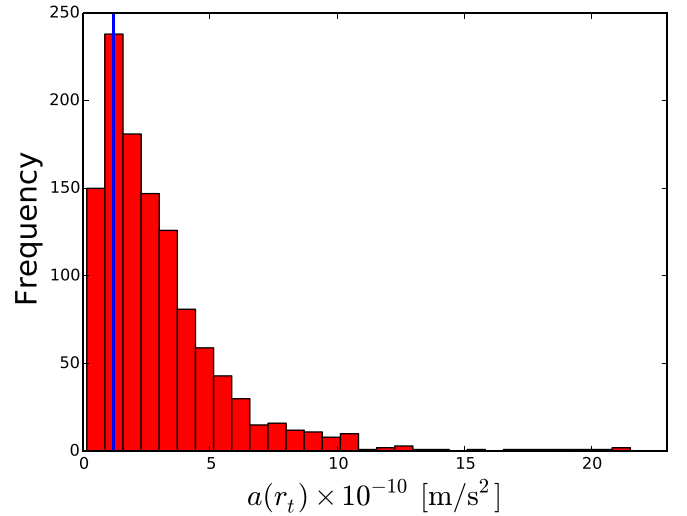


**Figure 4.** Acceleration at the transition radius  $r_t$  for the set of galaxies generated in model 2. The vertical line denotes  $a_0 = 1.2 \times 10^{-10} \text{ m s}^{-2}$  from MOND.

approach, because of the dependence of  $r_t$  on the geometry and mass distributions, it may seem at first that the  $g_{\text{N}}$  versus  $g_{\text{SI}}$  correlation should depend on the specifics of a particular galaxy, increasing the width of the correlation. The criterium for determining  $r_t$  in model 2 is the equality of the disk and bulge forces, and therefore of the accelerations. The bulge and disk mass distributions and characteristic lengths being correlated, the acceleration at  $r_t$  tends to cluster around a single value (see Figure 4). Because the  $g_{\text{N}}$  versus  $g_{\text{SI}}$  correlation is not sensitive to small variations of where the acceleration transition happens on the  $g_{\text{N}} = g_{\text{SI}}$  dashed line of Figure 1, any dependence on galaxy specificities is suppressed. In fact, a change of  $a_0$  by the variance extracted from Figure 4 does not appreciably affect Figure 1. We can quantitatively verify this by investigating whether large correlations exist between the galaxy characteristics and the residual shown in Figure 1. Large correlations would disagree with the **MLS2016** finding that their relation has no intrinsic width and with the further verification in Lelli et al. (2017) that the **MLS2016** residual does not correlate with galaxy properties. We used the Pearson correlation coefficient  $c_p$  to check for linear correlations between the residual and each galaxy property— $R_e$ ,  $h$ ,  $M_b$ , and  $M_d$ . Since the possible correlations could be nonlinear, we also used the Spearman  $c_s$  and Kendall  $c_k$  rank correlation coefficients. To maximize the sensitivity, we investigated the correlations at a fixed acceleration value, selected to be  $-11.1 \leq \log(g_{\text{N}}) \leq -11$ ; viz, we checked whether galaxy characteristics are correlated with  $g_{\text{SI}}$ , along the vertical line at  $\log(g_{\text{N}}) \approx -11$  for the simulated data shown in the bottom panel of Figure 1. The value  $\log(g_{\text{N}}) \approx -11$  is optimal because there, the width is large, which maximizes the sensitivity to possible correlations, while the statistics remain important. Selecting  $\log(g_{\text{N}}) \approx -11$  and computing correlation coefficients reveals that small correlations are present between the residual and the galaxy characteristics; see Figure 5 for an example with  $R_e$ . (The other galaxy characteristics  $h$  and  $M_b$  also display correlations, albeit smaller;  $M_d$  is not correlated.) To quantitatively investigate the effect of these correlations on the  $g_{\text{N}}$  versus  $g_{\text{N}}$  relation, we first take note that they are largely linear. This is suggested by the value of  $c_p$  being similar to  $c_s$ ,

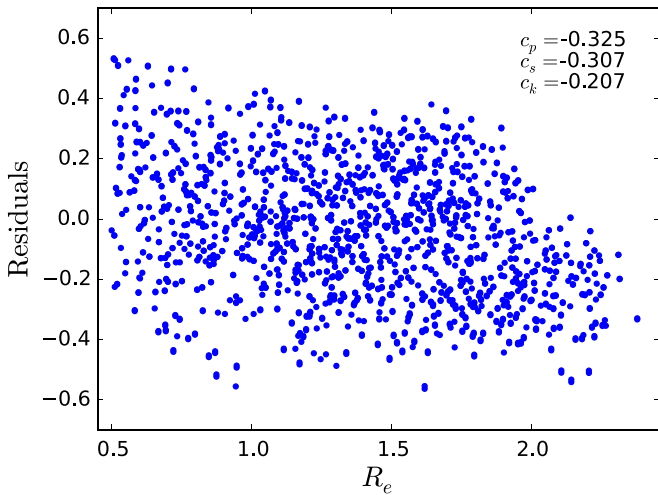


**Figure 5.** Bulge radius  $R_e$  vs. the residual between our calculated acceleration  $g_{SI}$  and the **MLS2016** relation, shown for  $\log(g_N) \approx -11$ . The Pearson’s ( $c_p = -0.325$ ), Spearman’s ( $c_s = -0.307$ ), and Kendall’s ( $c_k = -0.207$ ) correlation parameters, all with negligible  $p$ -values, indicate small correlations. Although they are clear, the correlations do not contribute significantly to the residual width.

and  $c_k$ , as well as by the fact that polynomial fits of the residual versus galaxy characteristic distribution are numerically close to a linear fit. The approximate linearity of the correlations is confirmed by fitting the correlations linearly, then removing the linear dependence using the fit result. While  $c_p$  calculated for the modified distributions must be zeroed by construction, the new  $c_s$  and  $c_k$  would reveal no remaining correlation only if the initial correlations had been linear. We indeed find negligible values of all of the correlation coefficients for the modified distributions, e.g.,  $c_p = -6 \times 10^{-17}$ ,  $c_s = -4 \times 10^{-3}$  ( $p$ -value 0.85), and  $c_k = -2 \times 10^{-3}$  ( $p$ -value 0.87) for  $R_e$ . By simultaneously applying this procedure for the distributions of the residual versus  $R_e$ ,  $h$ ,  $M_d$ , or  $M_b$ , we obtain an rms of 0.1812 for the modified residual distribution. Comparing with the rms for the initial residual distribution, 0.2101, we conclude that while the correlations are clear, as shown by their correlation coefficients and negligible  $p$ -values, their effects on the residual width are small, increasing it by 13%.

## 7. Discussion and Conclusion

Our findings support the possibility that GR’s self-interaction effects increase the gravitational force in large, nonisotropic mass distributions. When applied to disk galaxies, the increased force on the observed matter transposes to the missing mass needed in the traditional Newtonian analyses. We have thus proposed a plausible explanation for the correlation between the luminous mass in galaxies and their observed gravitational acceleration shown in **MLS2016**. That this correlation is encapsulated in our models, free of adjustable parameters, indicates its fundamental origin. This work also offers a possible explanation for the MOND acceleration scale  $a_0$ , showing that it dynamically emerges from galaxy baryonic mass distribution. Thus, in our approach, the emergence of  $a_0$  is due to complexity, rather than new physics, such as modifying gravity or Newton’s dynamical law.

The explanation for the origin of the **MLS2016** correlation that we propose here is natural in the sense that it is a consequence of the fundamental equations of GR and of the characteristic magnitudes of the galactic gravitational fields. As expected from such a natural explanation, no fine tuning of the

galaxy characteristic, nor free parameters, are necessary. This contrasts with the dark matter approach that necessitates both yet-unknown particles and a fine tuning in galaxy evolution and baryon–dark matter feedback (see, e.g., Ludlow et al. 2017). We used several approaches that are quite different, thus leading to a robust conclusion.

The work presented here adds to a set of studies that provide straightforward and natural explanations for the dynamical observations suggestive of dark matter and dark energy but without requiring them or modifying the known laws of nature. This includes flat rotation curves of galaxies (Deur 2009) and the evolution of the universe (Deur 2019). The Tully–Fisher relation (Tully & Fisher 1977) also finds an immediate explanation (Deur 2009). There are compelling parallels between those observations and QCD phenomenology, e.g., the equivalence between galaxies’ Tully–Fisher relation and hadrons’ Regge trajectories (Deur 2009, 2017), plausibly due to the similarity between GR’s and QCD’s underlying fundamental equations. The fact that these phenomena are well known for other areas of nature that possess a similar basic formalism, the current absence of a natural and compelling theory for the origin of dark matter (supersymmetry being now essentially ruled out), and the yet-unsuccessful direct detection of a dark matter candidate or its production in accelerators, despite coverage of the phase space expected for its characteristics, all support the approach we present here as a credible solution to the missing mass problem.

We are grateful to S. McGaugh for kindly sharing the raw data from his publication. We are thankful to A. Graham for helpful comments on the manuscript. This work was done in part with the support of U.S. National Science Foundation award Nos. 1535641 and 1847771.

## Appendix A

### Parallels between Galaxy Dynamics, Gravitation, and the Strong Interaction

The gauge theory of the nuclear strong interaction, QCD, is the archetype of an intrinsic nonlinear theory. The nonlinearities are intrinsic because they are present even in the pure-field case, that is, when matter is not present. This contrasts with electromagnetism (QED), which is linear for a pure field and for which nonlinearities appear only when matter fields are present. The same intrinsic nonlinearities as QCD are possessed by GR. In fact, the QCD field Lagrangian is topologically equivalent to that of the field part of the GR Lagrangian given in Equation (1). This is seen by developing the standard expression of the QCD Lagrangian density in terms of the gluon field strength  $F_{\mu\nu}$  as

$$\begin{aligned} \mathcal{L}_{\text{QCD}} = & -\frac{1}{4} F_{\mu\nu}^a F_a^{\mu\nu} = \frac{1}{4} (\partial_\nu A_\mu^a - \partial_\mu A_\nu^a) (\partial^\mu A^{\nu a} - \partial^\nu A^{\mu a}) \\ & + \sqrt{\pi} \alpha_s f^{abc} (\partial_\nu A_\mu^a - \partial_\mu A_\nu^a) A^{\mu b} A^{\nu c} \\ & - \pi \alpha_s f^{abe} f^{cde} A_\mu^a A_\nu^b A^{\mu c} A^{\nu d} + \text{matter term}, \end{aligned} \quad (\text{A1})$$

with  $A_\mu^a$  the gluon field and the SU(3) color index  $a = 1, \dots, 8$ . Here  $f^{abc}$  are the SU(3) structure constants, and  $\alpha_s$  is the QCD coupling. The matter term is the usual Dirac Lagrangian with a covariant derivative and color indices. With the bracket shorthand notation used for Equation (1), which now also includes summation over color indices, the QCD Lagrangian

has the form

$$\mathcal{L}_{\text{QCD}} = [dAdA] + \sqrt{16\pi\alpha_s} [A^2dA] - 4\pi\alpha_s [A^4] + \text{matter term.} \quad (\text{A2})$$

As for GR, the first term is the linear part of the theory, and the higher terms are the pure-field self-interaction vertices.

While GR and QCD have similar underlying fundamental equations for the pure-field part of their Lagrangians, they also have important differences.

(A) While QCD is a quantum field theory, GR is a classical field theory.

(B) The gravitational field is tensorial (spin 2), while QCD's field is vectorial (spin 1). Consequently, gravity is always attractive, while color charges in QCD can be attracted or repulsed.

(C) Here  $G$  is very small ( $GM_p^2 = 5.9 \times 10^{-39}$ , with  $M_p$  the proton mass), while  $\alpha_s$  is large ( $\alpha_s \approx 0.1$  at the transition between the weak and strong regimes of QCD; Deur et al. 2016).

However, these differences do not invalidate the parallel between QCD and GR in the context of astronomy.

Regarding difference A, classical effects are usually associated with Feynman tree diagrams, while quantum effects typically emerge from loop diagrams. The latter cause the scale evolution of the field coupling, while the former generate (in particular) field self-interaction. Thus, quantum effects are necessary for quark confinement, since they cause  $\alpha_s$  to increase enough so that the confinement regime is reached even with only a few color charges involved. However, the scale evolution of  $\alpha_s$  is not the basic mechanism for confinement.<sup>5</sup> It is the three- and four-gluon interaction tree diagrams that are at its root. In fact, bound states of QCD can be described semiclassically as divergences of perturbative (i.e., with a finite and relatively small value of the QCD coupling) expansion in ladder-type Feynman diagrams (Dietrich et al. 2013). Other semiclassical approaches to hadronic structure—which is ruled by QCD—exist, such as AdS/QCD (Brodszky et al. 2015), and efficiently reproduce the strong QCD phenomenology (Brodszky et al. 2010). To summarize, while quantum effects are necessary to enable the QCD confinement regime, the underlying mechanism for confinement is arguably classical.

The GR and QCD Lagrangians have identical tree diagrams, and thus GR, irrespective of its classical nature, should also exhibit effects akin to confinement once its effective field coupling  $\sqrt{GM}$  is large enough. In fact, black holes are fully confining solutions of GR.

Differences B and C essentially compensate for each other. Classically, a force coupling is truly constant, and  $G$ , in contrast to  $\alpha_s$ , remains small. However, a large effective field coupling can still occur, since the magnitudes of the fields are themselves large. They are proportional to  $\sqrt{M}$ , with  $M$  the mass of the field source. This ultimately arises from the tensorial nature of the gravity field, which makes it always attractive: gravitational effects can accumulate into large  $M$ , such as those characterizing galaxies. This effectively provides the large coupling in lieu of the (quantum) scale evolution of

<sup>5</sup> The apparent divergence of  $\alpha_s$  at a long distance due to scale evolution had led to an erroneous explanation of QCD's confinement in terms of the force coupling becoming infinite. However, the divergence is an artifact of applying a perturbative formalism in a nonperturbative regime, and this explanation for quark confinement is now disproven (Deur et al. 2016).

The analogous form of GR and QCD field Lagrangians, and the fact that large effective couplings are possible for both QCD and GR, may explain the intriguing similarities between observations suggestive of dark matter and dark energy and the phenomenology of hadronic structure:

1. Just like for hadrons, the total masses of galaxies and galaxy clusters appear much larger than the sum of their known constituent masses.

2. Hadrons and galaxies obey similar mass-rotation correlations (Regge trajectories, Regge 1959; and the Tully-Fisher relation, Tully & Fisher 1977, respectively. In both cases,  $J \propto M^a$ , with  $J$  the angular momentum,  $M$  the (baryonic) mass of the system, and  $a = 1.26 \pm 0.07$  or  $2$  for disk galaxies or hadrons, respectively. (The difference in the value of  $a$  is due to the difference in the system symmetry; see Deur 2017).

3. The large-scale arrangement of galaxies into filaments is reminiscent of QCD strings/flux tubes.

4. The nucleon and galaxy matter density profiles both decrease exponentially.

5. The approximate compensation at large scales between dark energy and matter's gravitational attraction—a phenomenon known as the cosmic coincidence problem—is comparable to the approximate suppression of the strong force at large distances, i.e., outside the hadron (Deur 2019).

These parallels and the similar form of QCD's and GR's Lagrangians suggest that very massive structures, such as galaxies or clusters of galaxies, have entered the nonlinear regime of GR, and that phenomena linked to the dark universe may be the consequence of neglecting this regime.

## Appendix B

### Summary of the Method Used in the Direct Calculations

The direct calculation of the effects of field self-interaction based on Equation (1) employs the Feynman path-integral formalism solved numerically on a lattice. While the method hails from quantum field theory, it is applied in the classical limit; see Deur (2017). The first and main step is the calculation of the potential between two essentially static ( $v \ll c$ ) sources in the nonperturbative regime. Following the foremost nonperturbative method used in QCD, we employ a lattice Carlo method (Deur 2009, 2017). The static calculations are performed on a 3D space lattice (in contrast to the usual 4D Euclidean spacetime lattice of QCD) using the 00 component of the gravitational field  $\phi^{00}$ . This implies that the results are taken to their classical limit, as will be explained below. Furthermore, the dominance of  $\phi^{00}$  over the other components of the gravitational field simplifies Equation (1) in which  $[\phi^n \partial_\mu \phi \partial^\mu \phi] \rightarrow a_n \phi^{00} \partial_\mu \phi \partial^\mu \phi$ , with  $a_n$  a set of proportionality constants. One has  $a_0 \equiv 1$ , and one can show that  $a_1 = 1$  (Deur 2017). In this appendix, we denote  $\phi \equiv \phi^{00}$ , and we will explicitly write  $h$  in the expressions in order to identify the quantum effects.

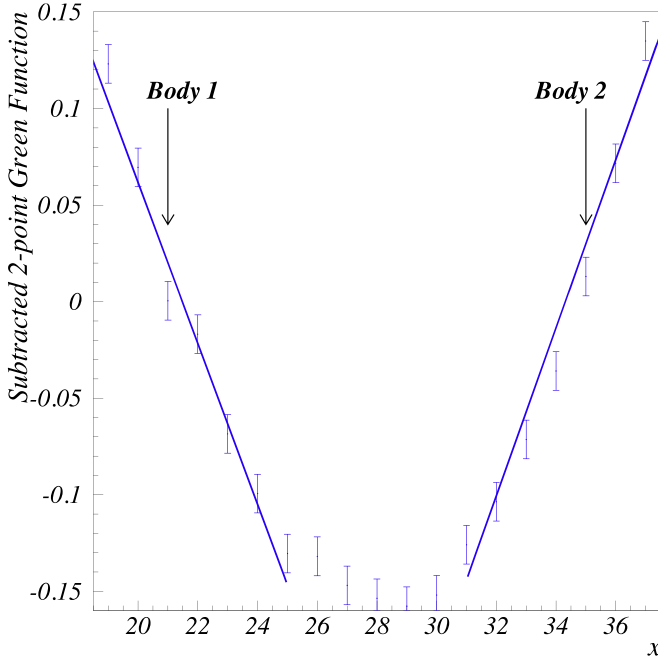


**Figure B1.** Potential around two massive bodies, with the  $1/x$  (free-field, Newtonian case) contribution subtracted. The straight lines demonstrate the approximate linear behavior of the potential away from the mid-distance between the bodies ( $x = 28$ ). There, by symmetry, the potential must flatten, as the calculation indeed shows. The potential was calculated in the static limit with Equation (1) for  $n \leq 2$ . The two sources are located on the  $x$ -axis at  $d = \pm 7$  lattice spacings  $u$  from the lattice center  $x = 28$ ,  $y = 0$ , and  $z = 0$ . The coupling is  $16\pi GM = 5.6 \times 10^{-5} u$ , the lattice size is  $N = 85$ , the decorrelation parameter (Deur 2017) is  $N_{\text{cor}} = 20$ , and  $N_s = 3.5 \times 10^4$  decorrelated paths were used. As boundary conditions, we used both random field values at the lattice edges, or Dirichlet boundary conditions. The resulting potentials are similar.

The instantaneous potential from a pointlike source located at  $x_1$  is given at location  $x_2$  by the two-point Green function  $G_{2p}(x_1 - x_2)$ . In the path-integral formalism,

$$G_{2p}(x_1 - x_2) = \frac{1}{Z} \int D\varphi \varphi(x_1) \varphi(x_2) e^{-iS_s/\hbar}, \quad (\text{B1})$$

where  $S_s \equiv \int d^4x \mathcal{L}$  is the action,  $Z \equiv \int D\varphi e^{-iS_s/\hbar}$ , and  $\int D\varphi$  is the sum over all possible field configurations. In the lattice method,  $Z \equiv 1$ . For Euclidean spacetime lattice simulations, one dimension is the time direction. Suppressing it by considering static or stationary systems allows us to identify  $G_{2p}$  to the instantaneous potential. In that case, the sum  $\int D\varphi$  is over configurations in position space only. This allows us to perform standard lattice calculations of difficult forces, such as gravity, in spite of its tensorial nature. The method described in the next paragraph is thus the standard one described in lattice textbooks.

Here  $G_{2p}(x_1 - x_2)$  is computed numerically on a cubic lattice of  $N^3$  sites to which a field of value  $\varphi$  is associated. The initial values of  $\varphi$  at each site are chosen randomly. The ensemble of the  $N^3$  values is known as a field configuration. A physical configuration should be such that  $S_s$  is minimized, viz the field verifies the Euler–Lagrange equations of motion. To numerically determine these proper configurations, one must first perform a Wick rotation:  $e^{-iS_s/\hbar} \rightarrow e^{-S_s/\hbar}$ . Euclidean and Minkowski actions being the same,  $S_s$  remains unchanged. One then follows the Metropolis algorithm iteratively:  $S_s$  is

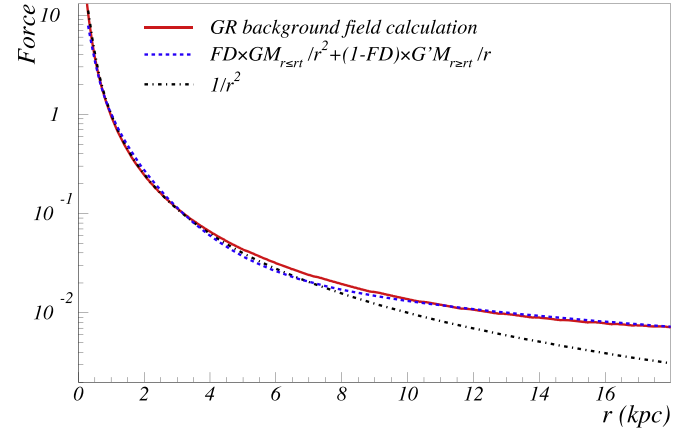


**Figure B2.** Distance dependence of the force obtained using a mean-field approximation to compute the self-interaction effects in a disk galaxy (solid red line; Deur 2020). The total galaxy baryonic mass is  $M_{\text{tot}} = 5 \times 10^{11} M_{\odot}$  and has an exponentially decreasing density profile characterized by  $h = 1.5$  kpc. The dashed blue line is a parameterization of the force using the same method as for model 1 described in the text; below a transition scale  $r_t = 2h$ , a Newtonian potential ( $1/r^2$  force) and a 2D logarithmic potential ( $1/r$  force) are used. A Fermi–Dirac function (FD) of width  $r_t$  is used to smoothly connect the two domains. Here  $M_{r \leq r_t}$  is the mass enclosed within  $r_t$ , and  $M_{r \geq r_t} = M_{\text{tot}} - M_{r \leq r_t}$  is the mass outside  $r_t$ . The dashed–dotted black line is the expectation from a pure Newtonian potential.

computed on each site. The value of  $\varphi$  at a given site is randomly varied, and the consequent modification  $\Delta S_s$  is calculated. If  $\Delta S_s \leq 0$ , the new  $\varphi$  value tends to minimize  $S_s$ . If so, one retains the new  $\varphi$  value, since the configuration is now closer to one obeying the equations of motion. If  $\Delta S_s > 0$ , one keeps the new  $\varphi$  if  $e^{-\Delta S_s/\hbar} > \epsilon$ , with  $\epsilon$  randomly chosen between zero and 1. Otherwise, the new  $\varphi$  is rejected. As one iterates the procedure over all of the sites, one converges to a configuration following the Euler–Lagrange equations; i.e., the configuration probability distribution obeys  $e^{-S_s/\hbar}$ . This operation is repeated and the results averaged until they converge and the statistical uncertainty inherent to the random method becomes small enough. Figure B1 shows an example of calculation that resulted in a linear potential around two forces, viz a constant force.

The path-integral formalism at the basis of the lattice approach produces intrinsically quantum results. However, the results used in the present manuscript are classical because the lattice time is taken to infinity (Buchmuller & Jakovac 1998), also known as the high-temperature limit. This can be understood as follows: since the system is static,  $S_s \equiv \int d^4x \mathcal{L} = \tau S$ , with  $S \equiv \int d^3x \mathcal{L}$  and  $\tau = \int_{t_0}^{\infty} dt \rightarrow \infty$ . The exponential of Equation (B1) becomes  $e^{-iS_s/\hbar} = e^{-i\tau S/\hbar}$ , and, just like  $\hbar \rightarrow 0$  suppresses quantum effects, the  $\hbar/\tau \rightarrow 0$  when  $\tau \rightarrow \infty$  yields the classical limit.

The method summarized in this appendix has been checked in different ways (Deur 2017).

1. Analytically known potentials for free fields (i.e., theories without self-interacting terms) have been recovered for both massive (Yukawa potential) or massless (Coulomb and Newtonian potentials) fields in three spatial dimensions. They were also satisfactorily verified in the two spatial dimensions case.
2. The analytically known potential (Frasca 2011) for the self-interacting  $\phi^4$  theory was retrieved.

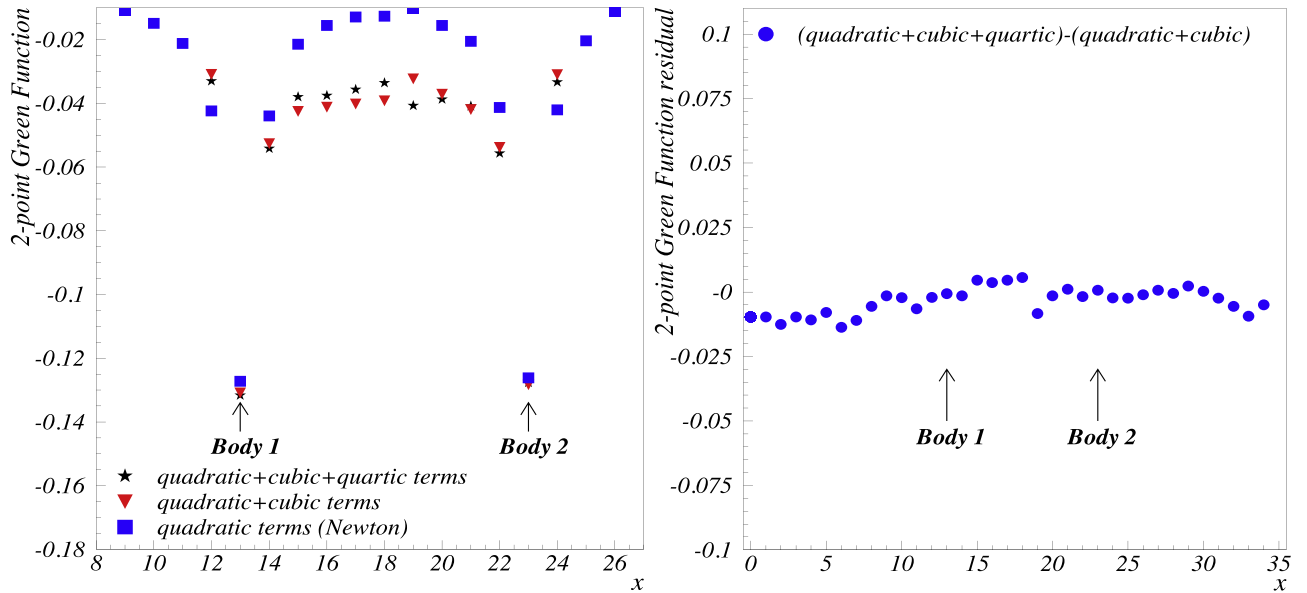


**Figure B3.** Left: potential between two massive bodies, calculated in the static limit with Equation (1) for  $n \leq 2$  (black stars),  $n \leq 1$  (red triangles), and  $n = 0$  (Newtonian case; blue squares). The two sources are located on the lattice  $x$ -axis at  $\pm 5$  lattice spacings  $u$  from the lattice center at  $x = 18$ ,  $y = 0$ , and  $z = 0$ . The coupling value is  $16\pi GM = 1 \times 10^{-4} u$ , the lattice size  $N = 35$ , the decorrelation parameter (Deur 2017) is 10, and  $N_s = 3 \times 10^4$  decorrelated paths were used. Random field values at the lattice edges were used for boundary conditions (similar results are obtained when using Dirichlet boundary conditions). With these calculation parameters, the difference between cases  $n \leq 2$  and  $n \leq 1$  is typically less than 10% of that between the  $n = 0$  and  $n \leq 1$  cases. Right: residual between the potential calculated with  $n \leq 2$  for Equation (1) and the one calculated for  $n \leq 1$ , shown with the same vertical scale range as that of the left panel for easier comparison. This residual is about  $\approx 10^{-3}$ , small compared to the  $n \leq 1$  and  $n \leq 2$  difference ( $4 \times 10^{-2}$  between the two bodies) and the potential scale (0.13). This justifies the truncation of Equation (1) to  $n = 2$ .

3. The phenomenological static potential for the strong interaction (Cornell potential; Eichten et al. 1975) was recovered once short-distance quantum effects, viz the scale dependence of  $\alpha_s$ , were accounted for.
4. The logarithmic potential resulting from the lattice calculation extended from a two-body system to a thin disk system was also obtained (Deur 2020) by estimating GR's self-interaction effects in a typical disk galaxy using a mean-field method that is not based on Equation (1); see Figure B2.

All of the GR lattice calculations were done with the Lagrangian given by Equation (1) with  $n = 0$ ,  $n \leq 1$ , and  $n \leq 2$ . In the static limit, the ratio of two consecutive field terms  $n$  and  $n + 1$  is  $(16\pi GM)^{1/2} \varphi_{00}$ , with  $16\pi GM \ll 1$  suggesting that Equation (1) can be truncated at low  $n$ . The  $n = 0$  results, which reproduce the expected free-field potentials, differ significantly from the  $n \leq 1$  and  $n \leq 2$  results once the system mass  $M$  is large enough (given the geometry of the system) so that GR has entered its nonlinear regime. However, the  $n \leq 1$  and  $n \leq 2$  calculations yielded similar results; see Figure B3. Thus, the first self-interaction term ( $n = 1$ ) dominates and is enough to describe the effects of field self-interaction. For smaller values of  $M$ , the  $n = 0$  contribution to the potential dominates the  $n > 0$  contributions.

### Appendix C

#### Nonuniversality of $G'$ and Its Value for Infinitely Thin Disks

The expression of the gravitational force confined in 2D is  $G'Mm/r$ . Therefore, one would naturally expect  $G'$  to be universal, like  $G$  in the 3D case. Furthermore, in the analogous QCD case, the effective coupling  $\sigma$  (the analog of  $G'$ ), known as the QCD string tension, is indeed universal with a value of

$0.18 \text{ GeV}^2$  (Deur et al. 2016). However,  $G'$  is not universal but rather depends on the geometry of the galaxy, its mass, and its density distribution.

To understand why, it is convenient to visualize a force as a field flux through an elementary surface. The force coupling constant controls the overall density of the field lines for a unit of charge or mass. Its value does not change the  $r$ -dependence of the force.<sup>6</sup> Likewise,  $G'$  determines the overall density of field lines passing through an elementary segment. This density depends on how early the transition from 3D to 2D occurs, as sketched in Figure C1, where, for clarity, we have drawn only the field lines emerging from the center of the galaxy, its densest locus. The transition occurs early for large disk densities or can be delayed by the presence of a spherically symmetric bulge. Therefore,  $G'$  depends on both the morphology and mass distribution of the galaxy components. In the case of an early transition (red lines in Figure C1), the field lines are denser and  $G'$  is large. For a later transition (blue lines), the field lines are sparser and  $G'$  is smaller. Thus,  $G'$  is not universal and approximately obeys  $G' = G/r_r$ .

In the QCD case,  $\sigma$  is universal because there is no geometrical or color charge variation; for the heavy meson case to which  $\sigma$  applies, two static pointlike sources of unit color charge are invariably considered, with the flavors of the sources and their type of color having no influence on the force. Therefore, the same distortion of field lines occurs, regardless of the type of meson considered, and  $\sigma$  is universal.

One may also ask what is the value of  $G'$  for a pure (bulgeless) disk, since there is no bulge-to-disk transition. Inside the disk, the mass distribution is approximately

<sup>6</sup> This is true only in the classical case. Running couplings in quantum field theory do affect the  $r$ -dependence because short-distance quantum effects are folded into the definition of the coupling (Deur et al. 2016). This definition of the coupling at quantum scale is conventional and, in any case, irrelevant here.

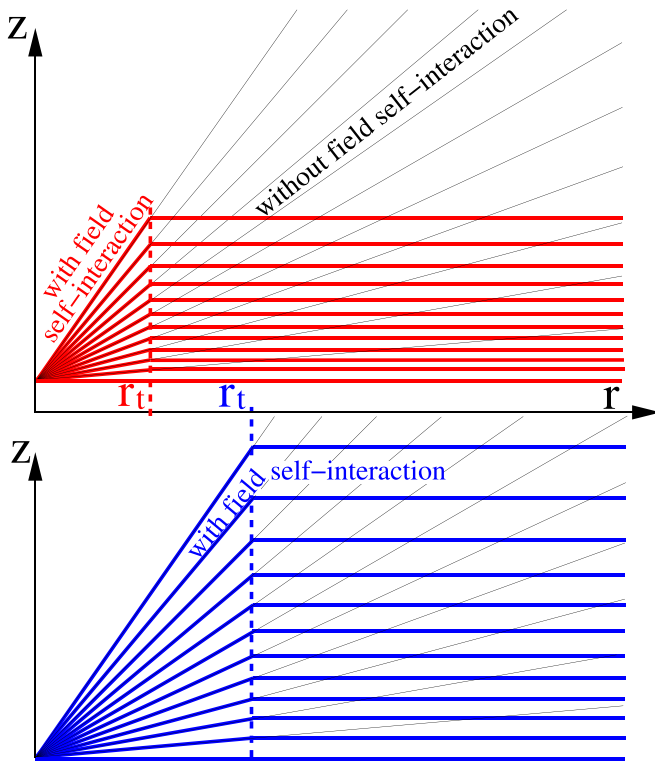


**Figure C1.** Dependence of  $G'$  on the transition scale  $r_t$ . Field lines emerge radially for a source (here, for clarity, only those emerging from the galaxy center are shown). A coupling constant, here  $G'$ , determines the density of the field lines emerging from the source (or, in this sketch, the number of field lines represented). Since the field possesses energy momentum, it interacts gravitationally with itself and with masses. Field self-interactions and interactions of the field with the massive disk in the  $z = 0$  plane bend the field lines. At smaller  $r$ , where the field lines are still radially distributed, the force behaves as  $1/r^2$  (3D regime). At larger  $r$ , where they are parallel to each other in a given vertical plane but still radially distributed in the disk plane—because of the cylindrical symmetry of the disk—the force behaves as  $1/r$  (2D regime). For simplicity, the transition distance between the two regimes is shown here to be infinitely short. For a small  $r_t$  (top panel), the field lines at large  $r$  are denser. For a larger  $r_t$  (bottom panel), the field lines are sparser. Their density is approximately proportional to  $r_t$ . Since a force coupling constant reflects the overall density of its field lines (i.e., ignoring the  $r$ -dependence), the coupling in the 2D case approximately obeys the  $G' = G/r_t$  assumed in this paper.

isotropic, so the scale height  $h_z$  of the disk sets a first limit for the scale; one expects  $r_t \propto h_z$ . However, considering an infinitely thin disk reveals that a transition scale  $r_t$  emerges dynamically, which may be larger than  $h_z$ . Even for an infinitely thin disk ( $h_z = 0$ ), it takes a length  $r_t$  for the initially radially distributed field lines to bend into parallel field lines. The mass and its distribution thus determine  $r_t$ ; the larger the mass and the more concentrated the density, the smaller  $r_t$ . The

dynamical emergence of  $r_t$  in a massive infinitely thin disk is analogous to the emergence of the confinement scale of QCD or the energy difference arising between the ground state and first excited levels in atoms or more complex materials in atomic or solid-state physics; viz, computing  $r_t$  is a spectral gap problem. The gap problem is notoriously difficult (Carlson et al. 2006) and without a known analytical solution. Therefore, even for infinitely thin disks,  $r_t$ —or, equivalently,  $G'$ —is nonuniversal and cannot presently be analytically calculated from first principles. It can be obtained from numerical calculations such as those in Deur (2009, 2017) or assessed phenomenologically, as done in this paper.

### ORCID iDs

Alexandre Deur <https://orcid.org/0000-0002-2203-7723>  
 Corey Sargent <https://orcid.org/0000-0003-3217-9984>  
 Balša Terzić <https://orcid.org/0000-0002-9646-8155>

### References

- Brodsky, S. J., de Teramond, G. F., & Deur, A. 2010, *PhRvD*, **81**, 096010  
 Brodsky, S. J., de Teramond, G. F., Dosch, H. G., & Erlich, J. 2015, *PhR*, **584**, 1  
 Buchmuller, W., & Jakovac, A. 1998, *NuPhB*, **521**, 219  
 Caon, N., Capaccioli, M., & D'Onofrio, M. 1993, *MNRAS*, **265**, 1013  
 Carlson, J., Jaffe, A., & Wiles, A. 2006, *The Millennium Prize Problems* (Providence, RI: American Mathematical Society)  
 Deur, A. 2009, *PhLB*, **676**, 21  
 Deur, A. 2014, *MNRAS*, **438**, 1535  
 Deur, A. 2017, *EPJC*, **77**, 412  
 Deur, A. 2019, *EPJC*, **79**, 883  
 Deur, A. 2020, arXiv:2004.05905  
 Deur, A., Brodsky, S. J., & de Teramond, G. F. 2016, *PrPNP*, **90**, 1  
 Dietrich, D. D., Hoyer, P., & Järvinen, M. 2013, *PhRvD*, **87**, 065021  
 Eichten, E., Gottfried, K., Kinoshita, T., et al. 1975, *PhRvL*, **34**, 369  
 Einstein, A., Infeld, L., & Hoffmann, B. 1938, *AnMat*, **39**, 65  
 Fierz, M., & Pauli, W. 1939, *RSPSA*, **173**, 211  
 Frasca, M. 2011, *JNMP*, **18**, 291  
 Graham, A. W., & Worley, C. C. 2008, *MNRAS*, **388**, 1708  
 Khosroshahi, H. G., Wadadekar, Y., & Kembhavi, A. 2000, *ApJ*, **533**, 162  
 Lelli, F., McGaugh, S. S., Schombert, J. M., & Pawłowski, M. S. 2017, *ApJ*, **836**, 152  
 Ludlow, A. D., Benítez-Llambay, A., Schaller, M., et al. 2017, *PhRvL*, **118**, 161103  
 McGaugh, S. S., Lelli, F., & Schombert, J. M. 2016, *PhRvL*, **117**, 201101  
 Méndez-Abreu, J., Aguerrí, J. A. L., Corsini, E. M., & Simonneau, E. 2008, *A&A*, **487**, 555  
 Milgrom, M. 1983, *ApJ*, **270**, 365  
 Padmanabhan, T. 2008, *IJMPD*, **17**, 367  
 Regge, T. 1959, *NCim*, **14**, 951  
 Salam, A. 1974, *IC/74/55*, <http://inspirehep.net/record/90219>  
 Sérsic, J. L. 1963, *BAAA*, **6**, 41  
 Sofue, Y. 2015, *PASJ*, **68**, 2  
 Tully, R. B., & Fisher, J. R. 1977, *A&A*, **54**, 661  
 Zee, A. 2013, *Einstein Gravity in a Nutshell* (Princeton, NJ: Princeton Univ. Press)